

Improving Damped Random Walk parameters for SDSS Stripe82 Quasars with baseline extension with PanStarrs1 data.

KRZYSZTOF L. SUBERLAK,¹ ŽELJKO IVEZIĆ,¹ AND CHELSEA MACLEOD²

¹*Department of Astronomy
University of Washington
Seattle, WA 98195, USA*

²*Harvard Smithsonian Center for Astrophysics
60 Garden St, Cambridge, MA 02138, USA*

(Received January 1, 2019; Revised January 17, 2019; Accepted February 1, 2019)

Submitted to ApJ

ABSTRACT

1. INTRODUCTION

Quasars are inherently variable sources at the rms level of 0.2 mag. They are distant active galactic nuclei, harboring a supermassive black hole surrounded by a hot accretion disk. Although it is agreed upon that majority of optical emission stems from the accretion disk, the detailed origin of variability has been debated over the past 50 years. Some favor a thermal origin of variability (Kelly et al. 2013), related to the propagation of inhomogeneities (“hot spots”) in the disk (Dexter & Agol 2011), others suggested magnetically elevated disks (Dexter & Begelman 2019), or X-ray reprocessing (Kubota & Done 2018). Quasar light curves have been successfully described using the Damped Random Walk (DRW) model (Kelly et al. 2009; MacLeod et al. 2010; Kozłowski et al. 2010; Zu et al. 2011; Kasliwal et al. 2015), and the DRW parameters have been linked to the physical quasar properties. MacLeod et al. (2010) (M10) found correlations of the characteristic timescale and variability amplitude to the black hole mass, and quasar luminosity.

Variability is also a classification tool, allowing to distinguish quasars from other variable sources that do not exhibit such stochastic variability pattern (MacLeod et al. 2011). Using the DRW parametrization, (MacLeod et al. 2011) found that DRW timescale and amplitude for QSO are order of magnitude different from stars. This is especially useful for selecting quasars in the intermediate redshift range (which overlaps the stellar locus in color-color diagrams - see Sesar et al.

2007; Yang et al. 2017). Variability has also been used to increase the completeness in measurements of Quasar Luminosity Function (see Ross et al. 2013; Palanque-Delabrouille et al. 2013; AlSaiyad 2016; McGreer et al. 2013, 2018).

Due to its stochastic nature, the DRW process requires the light curve to be many times longer than the characteristic timescale for an unbiased parameter retrieval. The rule of thumb is that the light curve must be at least ten times longer than its characteristic timescale (Kozłowski et al. 2010; Kozłowski, Szymon 2017). For this reason some studies have restricted the probed redshift range, limiting the quasar sample to where one would expect only shorter timescales based on previous studies (Sun et al. 2018; Guo et al. 2017). Others have suffered from short-baseline biases by employing single-survey data (Hernitschek et al. 2016). Thus by extending available quasar light curves we are able to better recover a wider range of DRW timescales, and probe a wider range of redshifts and black hole masses.

Almost a decade ago MacLeod et al. (2010) (hereafter M10) published their research using the SDSS Stripe 82 data, and new datasets (PS1,PTF,CRTS) have become available since that can extend the quasar light curves by almost 50% . Indeed, (Li et al. 2018) combined SDSS and Dark Energy Camera Legacy Survey (DECaLS) data, to provide a 15 year baseline, but by focusing on a large area to encompass as many quasars as possible (119,305 up to $z=4.89$) suffered from having to employ an ensemble approach (SF) rather than the direct light curve modelling due to poor sampling. On the other hand, (Sánchez-Sáez et al. 2018) who employed optical data from QUEST-La Silla AGN variability survey, also used the Structure Function parametrization

(amplitude of variability and the excess variance), because the light curve length (less than 5 years for 2435 quasars) excluded the possibility of unbiased retrieval of characteristic timescale.

This paper improves on the DRW parameters (Section 2) describing amplitude and characteristic timescale of Stripe82 quasars by extending the SDSS light curves for well-sampled Stripe82 with PanStarrs1 (PS1) data (Section ??). We revisit trends between the DRW parameters and physical quasar properties, such as black hole mass, or bolometric luminosity (Section 5). We make predictions for fidelity of DRW parameter retrieval once ZTF and LSST data become available.

2. METHODS

2.1. DRW as a Gaussian Process

DRW (OrnsteinUhlenbeck process) can be understood as a member of a class of Gaussian Processes (GP). Each GP is described by a kernel - a covariance function that contains a measure of correlation between two points x_n, x_m , separated by Δt_{nm} . For the DRW process, the kernel is

$$k(\Delta t_{nm}) = a \exp(-\Delta t_{nm}/\tau) \quad (1)$$

$$= \sigma^2 \exp(-\Delta t_{nm}/\tau) \quad (2)$$

$$= \sigma^2 ACF(\Delta t_{nm}) \quad (3)$$

Here a or σ^2 is an amplitude of correlation decay as a function of t_{nm} , while τ is the characteristic timescale over which correlation drops by $1/e$. For a DRW, the correlation function $k(\Delta t_{nm})$ is also related to the autocorrelation function ACF .

Related to $k(\Delta t_{nm})$ is the structure function of the DRW process (see MacLeod et al. (2012); Bauer et al. (2009); Graham et al. (2015) for an overview), which expresses the rms of magnitude differences Δm as a function of temporal separation Δt , is :

$$SF(\Delta t) = SF_\infty (1 - \exp(-|\Delta t|/\tau))^{1/2} \quad (4)$$

where SF_∞ is the asymptotic value of SF for large time lags. It is known that for QSOs SF follows approximately power law, $SF \propto \Delta t^\beta$, and it levels out for large Δt (see MacLeod et al. (2012)). Note that $SF_\infty = \sqrt{2}\sigma$ in the above.

To estimate the DRW parameters and fit simulated or real data we employ Celerite - a new fast GP modelling tool (Foreman-Mackey et al. 2017). Combined with the DRW kernel this is similar to the method used by Rybicki & Press (1992); Kozłowski et al. (2010), M10 - like in previous work, we use a prior on σ and τ uniform in

log space. The main difference is that rather than adopting the Maximum A-Posteriori (MAP) as the 'best-fit' value for sought parameters, we find the expectation value of the marginalized log posterior. If the posterior space was a 2D Gaussian in σ, τ space, the expectation value would coincide with the maximum of the log posterior. However, due to non-Gaussian shape of the log posterior, we find that the expectation value is a better estimate of σ and τ rather than MAP.

2.2. The impact of light curve baseline

Kozłowski, Szymon (2017) reports that one cannot trust any results of DRW fitting unless the light curve length is at least ten times longer than the characteristic timescale. We confirm these generic trends by repeating his simulation setup. We model 10 000 DRW light curves with fixed length (baseline) $t_{exp} = 8$ years, $SF_\infty = 0.2$ mag, sampling over a range of input timescales. With a fixed baseline, we are thus exploring a range of ρ : the ratio of timescale to baseline ($\rho = \tau/t_{exp}$, $\rho \in \{0.01 : 15\}$). Fig. ?? each of 100 distinct values of ρ we perform 100 light curve realizations, thus

To simulate observational conditions we add to the true underlying signal $s(t)$ a noise offset, $n(t)$. Like Kozłowski, Szymon (2017), we assume $n(t)$ to be drawn from a Gaussian distribution $\mathcal{N}(0, \sigma(t))$ with a width $\sigma(t)$, corresponding to the photometric uncertainty at the given epoch, $e(t)$:

$$y(t) = s(t) + n(t) \quad (5)$$

The $s(t)$ is found by iterating over the array of time steps t . At each step, we draw a point from a Gaussian distribution, for which the mean and standard deviation are re-calculated at each timestep. Starting at t_0 , the signal is equal to the mean magnitude, $s_0 = m$. After a timestep $\Delta t_i = t_{i+1} - t_i$, the signal s_{i+1} is drawn from $\mathcal{N}(loc, stdev)$, with :

$$loc = s_i e^{-r} + m (1 - e^{-r}) \quad (6)$$

and

$$stdev^2 = 0.5 SF_\infty^2 (1 - e^{-2r}) \quad (7)$$

where $r = \Delta t_i/\tau$, τ is the damping timescale, SF_∞ is the variability amplitude, and m the mean magnitude. This follows the formalism in Kelly et al. (2009) (eqs. A4 and A5) as well as in MacLeod et al. (2010) (Sec. 2.2), and is equivalent to the setup of Kozłowski, Szymon (2017).

We adopt SDSS S82-like cadence with $N=60$ epochs, or OGLE-III like cadence with $N=445$ epochs. The errors were set by the adopted mean magnitudes, $r = 17$ and $I = 18$, as in Kozłowski, Szymon (2017) :

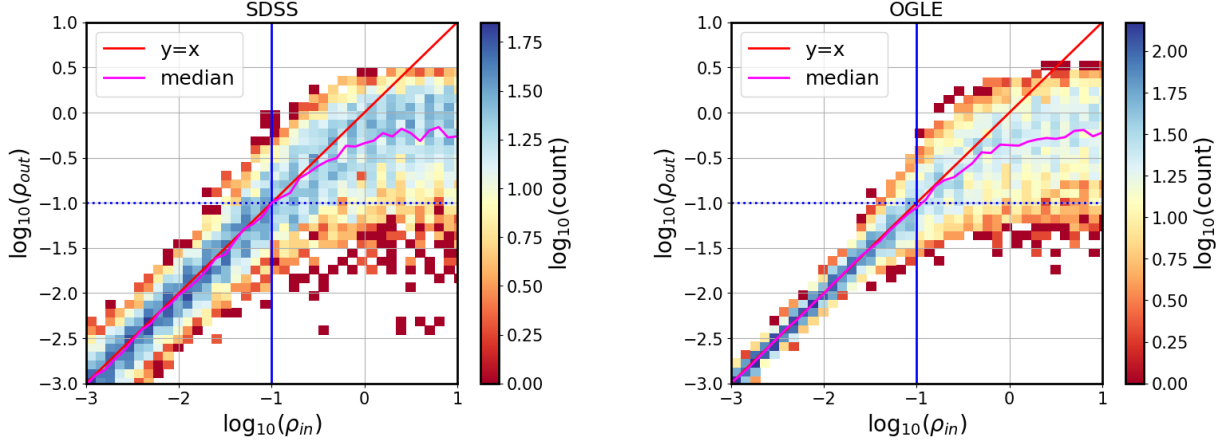


Figure 1. Probing the parameter space of $\rho = \tau / t_{exp}$, with a simulation of 10 000 light curves : 100 light curves per each of 100 ρ values spaced uniformly in logarithmic space between $\rho \in \{0.01 : 15\}$. Thus with the baseline t_{exp} set to 8 years, we sample a range of 100 input timescales, as in Kozłowski, Szymon (2017). Left panel shows the SDSS-like cadence with $N=60$ points, and the right panel OGLE-like cadence with $N=445$ points. The dotted horizontal and solid vertical lines represent $\rho = 0.1$, i.e. the baseline is ten times longer than considered timescale. The diagonal line is $y = x$, i.e. the line that would be followed if the recovered ρ (τ) was exactly the same as the input ρ (τ).

$$\sigma_{SDSS}^2 = 0.013^2 + \exp(2(r - 23.36)) \quad (8)$$

$$\sigma_{OGLE}^2 = 0.004^2 + \exp(1.63(I - 22.55)) \quad (9)$$

Fig 1 shows that as stipulated in Kozłowski, Szymon (2017), the recovered ρ becomes meaningless ('unconstrained') if the available baseline is not at least ten times longer than the underlying timescale. It also means that by extending the baseline we can move from the biased region to the unbiased regime. Encouraged by this result, we extend the baselines of quasar light curves, and revisit relations studied by M10 and Harnitschek et al. (2016).

3. DATA

3.1. Surveys

We focus on data pertaining to a 290 deg² region of southern sky, repeatedly observed by the SDSS between 1998 and 2008. Originally aimed at supernova discovery, objects in this area, known as Stripe82 (S82), were re-observed on average 60 times (see MacLeod et al. 2012 Sec. 2.2 for overview, and Annis et al. 2014 for details). Availability of well-calibrated (Ivezić et al. 2007), long-baseline light curves spurred variability research (see Sesar et al. 2007). The catalog prepared by (Schneider et al. 2008) as part of DR9 contains 9258 spectroscopically confirmed quasars.

We extend the SDSS light curves with PanSTARRS (PS1) (Chambers 2011; Flewelling 2018), CRTS (Drake et al. 2009), and PTF (Rau et al. 2009). We find 9248 PS1 matches, 6455 PTF matches, and 7737 CRTS matches to SDSS S82 quasars. There are 6444 quasars

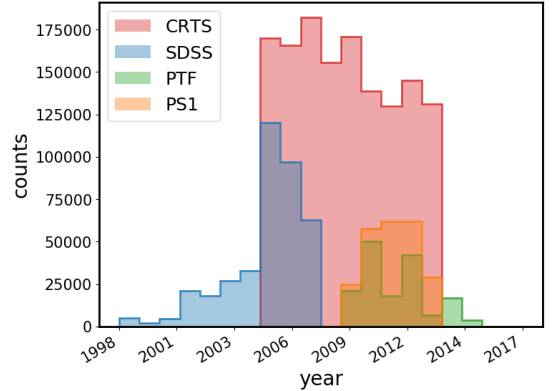


Figure 2. Raw photometric measurements for quasars in Stripe 82 from SDSS(r), PS1(gri), PTF(gR), CRTS(V).

with SDSS-PS1-PTF-CRTS data. Fig. 2 shows the distribution of raw epochs, and Fig 3 the baseline coverage of various surveys. Each survey uses a unique set of bandpasses and cadences : SDSS light curves contain near-simultaneous $\{u, g, r, i, z\}_{SDSS}$, and the other are non-simultaneous : $\{g, r, i, z, y\}_{PS1}$, $\{g, R\}_{PTF}$, V_{CRTS} .

3.2. Photometric offsets

To utilize all data we define a common 'target' bandpass. SDSS r band is closest to PS1 r, PTFr, CRTSV. For this reason we translate photometry from nearby filters ($\{g, R\}_{PTF}$, $\{g, r, i\}_{PS1}$, V_{CRTS}) to the 'master' r_{SDSS} band.

With two photometric systems, eg. SDSS(ugriz), and PS1(grizy), we can find offsets (or color terms) from one to another. Consider SDSS as target system, PS1 as

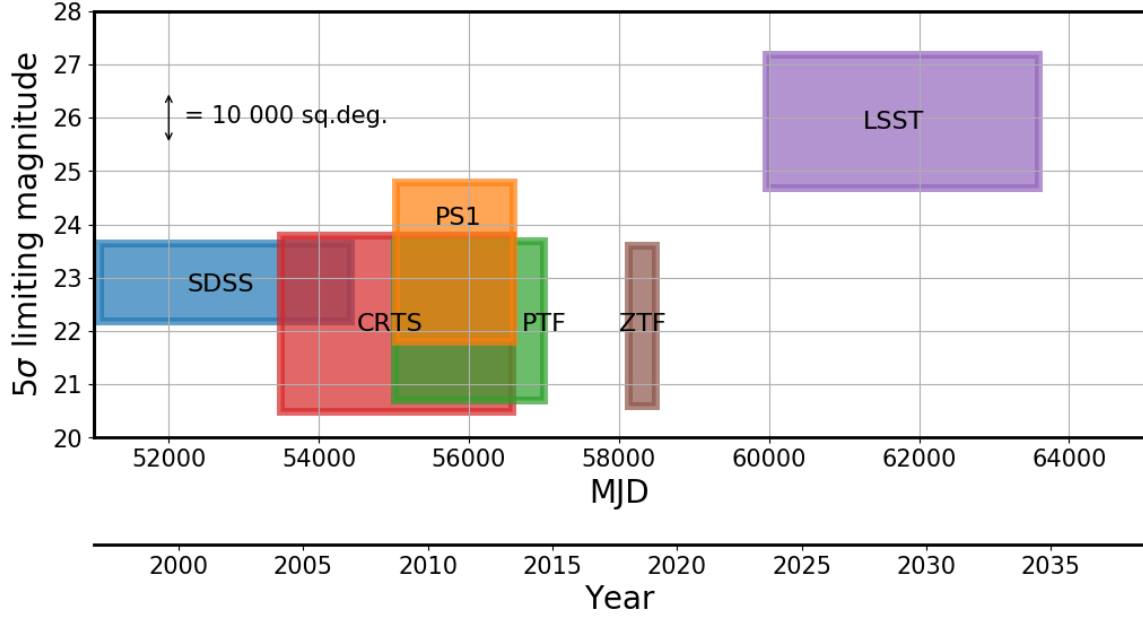


Figure 3. An illustration of survey baseline, sky area covered, and depth. The width of each rectangle corresponds to the extent of light curves available (or simulated) for Stripe 82 quasars for each survey. For SDSS this means DR7; for CRTS DR2, PS1 DR2, PTF DR2, ZTF year 2018, and LSST the full 10-year survey. The lower edge of each rectangle corresponds to the 5σ limiting magnitude (SDSS r, PS1 r, PTF R, ZTF r, LSST r, CRTS V). The vertical extent corresponds to the total survey area (for SDSS, up to and including DR15). Note how PS1 and PTF extend the baseline of SDSS by approximately 50%, and how inclusion of LSST triples the SDSS baseline. For reference, the area covered by LSST is 25000 sq.deg., which corresponds to 60% of the sky. The whole sky has an area of 4π steradians (41253 sq.deg.).

the auxiliary system, so that we find offsets from PS1 to SDSS. This amounts to creating ‘synthetic’ SDSS bands from PS1, using the SDSS color to spread the stellar locus. More generally, we would always use the color of the target system :

$$r_{PS1} - r_{SDSS} = f(SDSS(g-i)) \quad (10)$$

the function is a polynomial fitted to the stellar locus on the plot of $SDSS(g-i)$ vs $r_{PS1} - r_{SDSS}$. We use $SDSS(g-i)$ because it provides a larger wavelength baseline than $(g-r)$.

Note that there are other possible choices for the target band and the intermediate color to spread the stellar locus. For instance, rewriting the above as $m-s = f(x)$, Tonry et al. (2012) derived offsets from SDSS to PS1 using $x = SDSS(g-r)$, $m = PS1\{g, r, i, z, y\}$, and $s = SDSS(r)$.

Since quasars occupy a blue region in the color-color diagram (Fig. 4), we calculate photometric offsets specifically for this region of the spectrum. We only show the color-magnitude diagrams for PS1 offsets (Fig. 5) since we choose not to include CRTS and PTF data in the final sample.

The offsets used to make combined r-band light curves are shown in Table 1

4. SIMULATION : LESSONS LEARNED

Having established in Sec. 2.2 that extending the light curve baseline improves the recovery of input DRW parameters, we combine SDSS light curves with PS1 data. We first consider the theoretical improvement in the fit, simulating DRW light curves for which we select SDSS-PS1, or SDSS-only sections. Then we fit the real data with DRW model, and divide by $(1+z)$ to study the timescales in rest frame.

We simulate the DRW using the real cadences and errors corresponding to sections of combined light curves (SDSS, PS1, CRTS, PTF), including the portion corresponding to the predicted LSST and ZTF contribution. For LSST segment we assumed a cadence of 50 epochs per year, for 10 years (between 2023-2033), and magnitude-dependent photometric uncertainty from Sec. 3.5 in LSST Science Collaboration et al. (2009):

$$\sigma_{LSST}(m)^2 = \sigma_{sys}^2 + \sigma_{rand}^2 \text{ (mag)}^2 \quad (11)$$

$$\sigma_{rand}^2 = (0.04 - \gamma)x + \gamma x^2 \quad (12)$$

$$x = 10^{0.4(m-m_5)} \quad (13)$$

with $\sigma_{sys} = 0.005$, $\gamma = 0.039$, $m_5 = 24.7$ (see Table 3.2 therein).

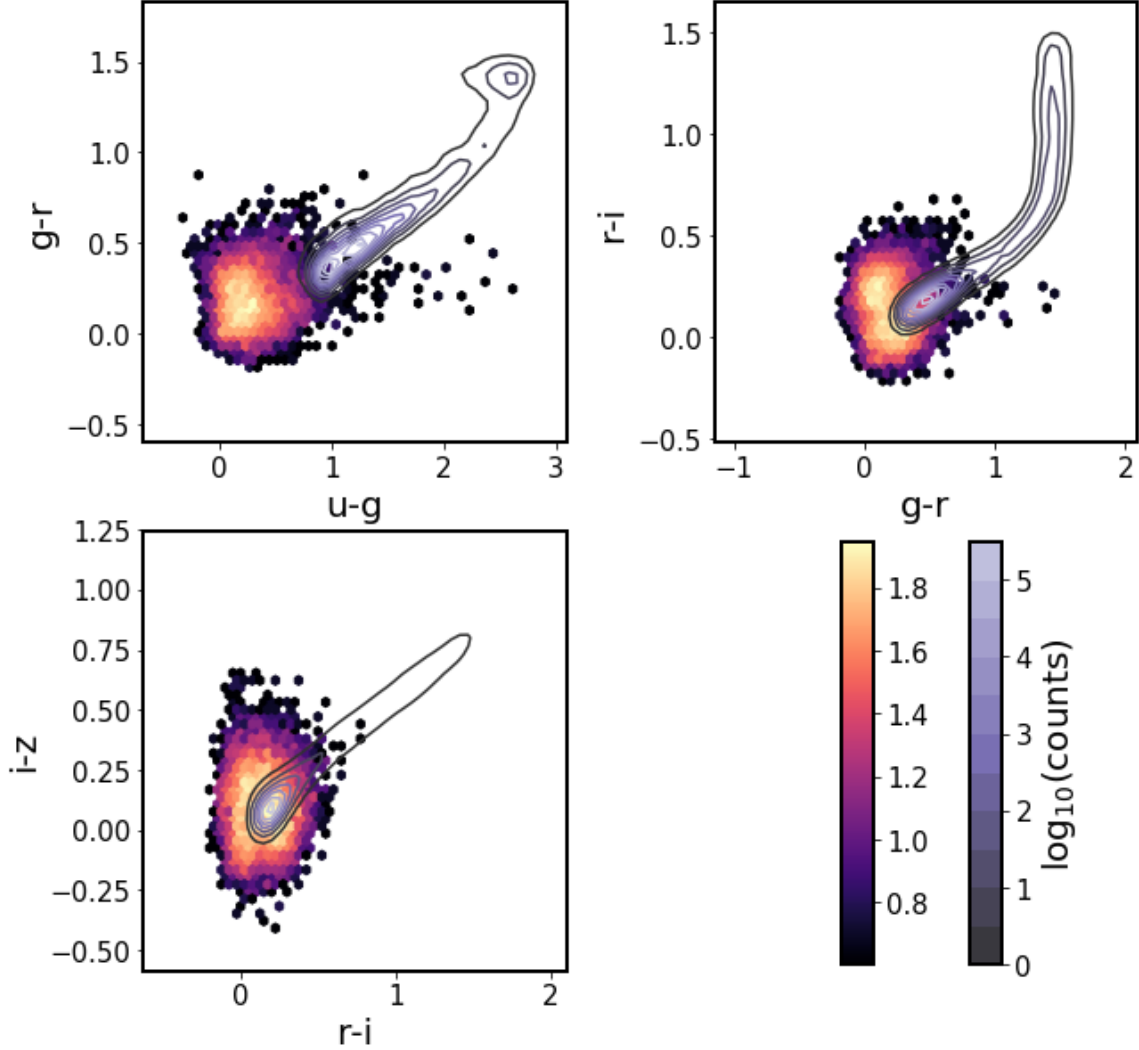


Figure 4. Regions occupied in color-color space by S82 quasars (colors) and standard stars (contours) (Schneider et al. 2010). We show only 10 000 randomly chosen stars from the full 1 mln + standard stars catalog Ivezić et al. 2007.

For the ZTF segment (the 2018 data that covers Stripe82, to be released May 9 2019), we have assumed 120 observations in ZTFg and ZTFr, every three days, with error structure derived from ZTF light curves. We fitted the functional form described above to estimate the ZTF photometric uncertainty (see Fig. 6)

For all light curves we assumed $\tau = 575$ days, $SF_{\infty} = 0.2$ mag (the median of S82 distribution in MacLeod et al. (2010)). Fig. 7 shows an example simulated DRW for SDSS-PS1-LSST.

To the simulated true DRW signal we add Gaussian noise corresponding to epochal heteroscedastic errors (eg. for SDSS epochs we use SDSS errors, for PS1 epochs we use PS1 errors, etc). This noise causes the underlying signal to become less constrained for larger errors (eg. CRTS and PTF portion). We further found that inclusion of ZTF data for 2018 would not significantly

change our results. Inclusion of PS1 data with its excellent photometric uncertainty (as compared to ZTF or PTF) is the best improvement over existing SDSS results. We predict that in the future (after more data has been assembled and re-calibrated) ZTF will help, but not as dramatically as LSST (see Fig. 9). For this reason we found that using only SDSS-PS1 portion is the best tradeoff between adding more baseline vs introducing more uncertainty by noisy simulation - see Fig. 8 for error distribution, and Fig. 7 for illustration of the simulated light curve.

In accordance with Fig. 1, we find that extending the baseline decreases the bias in retrieved DRW parameters. Indeed, Fig. 9 shows that for an ensemble of 6444 simulated light curves the recovered DRW parameters become less biased when supplementing the SDSS data with PS1. , and th and 10

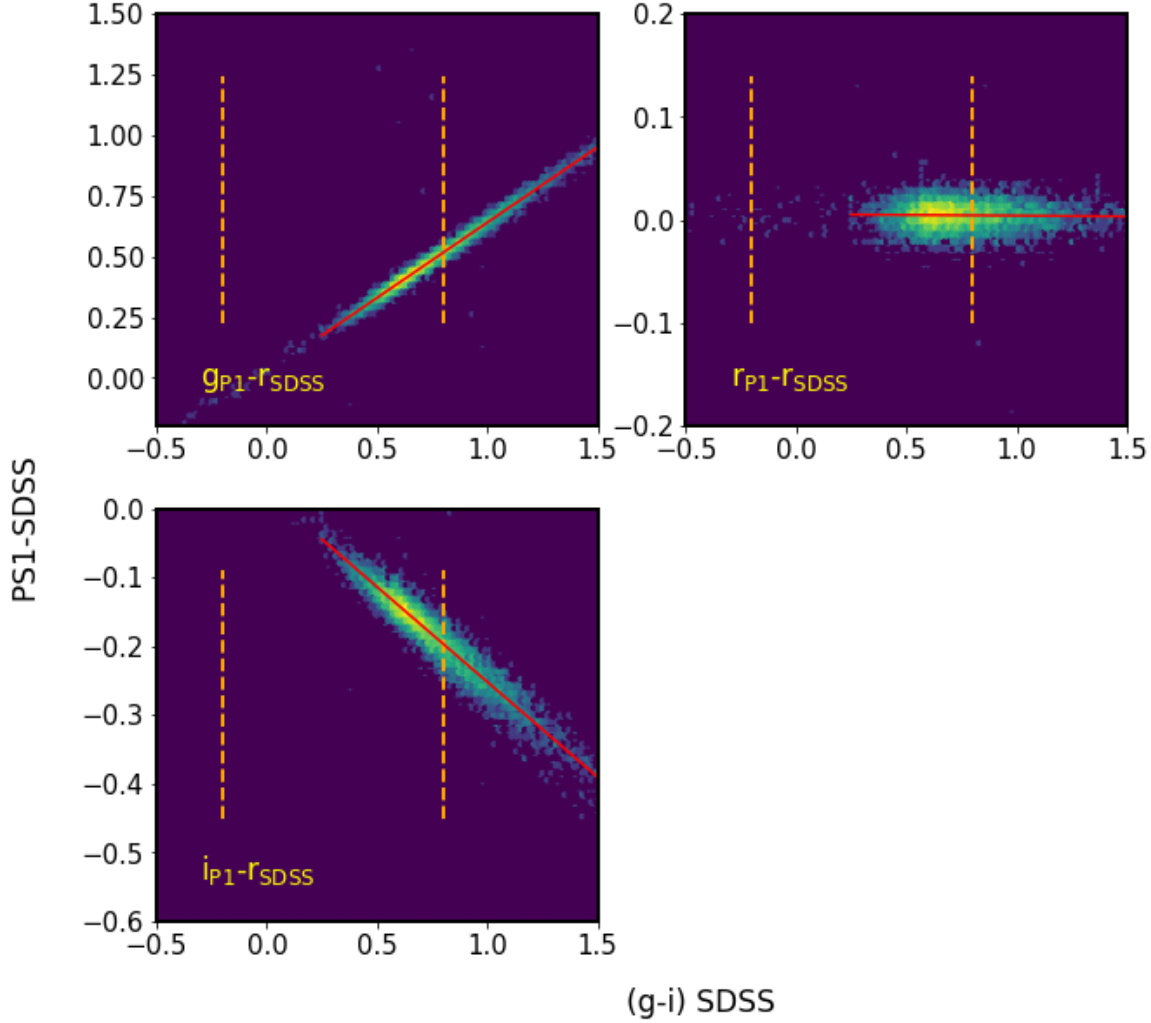


Figure 5. The SDSS-PS1 offsets. We plot only bright stars that have $\text{SDSS}(r) \leq 19$, and that fulfill $\text{mErr} * \sqrt{\text{Nobs}} \leq 0.03$. Each panel plots about 6000 stars of the 47000 CRTS S82 stars. Vertical dashed lines mark the region in SDSS color space occupied by quasars (see Fig. 4), used to fit the stellar locus with a polynomial.

5. RESULTS: FITTING SDSS-PS1 WITH CELERITE

We have extended the baseline of Stripe82 quasars by adding to SDSS r-band data the PS1 g,r,i data, transformed into common SDSS r-band. Encouraged by the simulation results we first show that the fitting routine is consistent when using only SDSS r-band portion with the results obtained by M10. Since the variability is assumed to be intrinsic to quasars, we shift timescales to rest frame : $\tau_{\text{RF}} = \tau_{\text{OBS}} / (1 + z)$. First, fits for DRW parameters using only the SDSS segment of quasar light curves (τ_{SDSS} , $SF_{\infty, \text{SDSS}}$) are consistent with M10 : Fig. 11 shows that the distributions τ_{RF} and SF_{∞} overlap. Furthermore, Fig. 12 compares DRW parameters using only the SDSS segment for M10 and this work, plotting the ratio of M10 results to σ_{SDSS} , τ_{SDSS} . Both

histograms are peaked close to 0 which would indicate perfect agreement.

5.1. Trends with Rest-frame Wavelength

Following MacLeod et al. (2011), we shift all timescales to rest-frame, and prior to looking for correlations with physical quantities (black hole mass, luminosities, redshifts), we correct all quantities to rest frame wavelength of 4000\AA . This is because originally the SDSS data employed by MacLeod et al. (2011) were taken in near-simultaneous ugriz filters, each centered on different observers wavelength. Because quasars are not all at the same distance, this means that the same band would probe a different rest-frame wavelength for each quasar. MacLeod et al. (2011) found that τ_{RF} and $SF_{\infty}(f)$ can be connected to rest-frame wavelength λ_{RF} via power law :

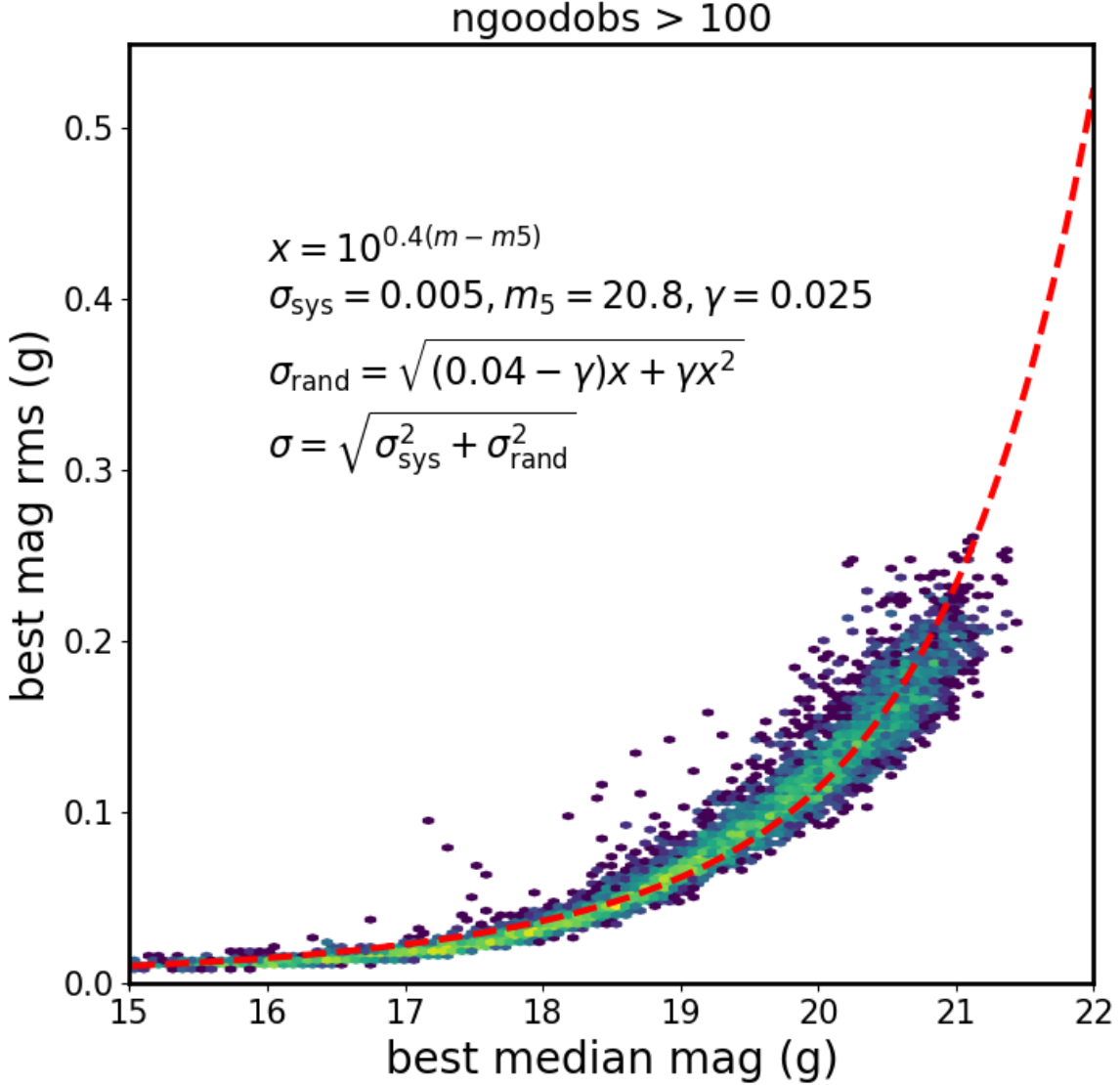


Figure 6. The rms spread as a function of magnitude for ZTF objects with over 100 observations. We overplot the functional describing the adopted error model. Properties of ZTF photometric uncertainty are largely similar to the PTF uncertainties.

$$f \propto \left(\frac{\lambda_{RF}}{4000\text{\AA}} \right)^B \quad (14)$$

Fig. 13 shows that both using SDSS and SDSS-PS1 the timescales and asymptotic amplitudes follow approximate power law coefficients found by MacLeod et al. (2011).

5.2. Trends with Luminosity, Black Hole Mass, and Redshift

Here we examine the main scientific results : the correlations between variability parameters ($\tau, SF\infty$), and the physical properties of quasars (rest-frame wavelength λ_{RF} , redshift z , absolute i-band magnitude M_i , and black hole mass M_{BH}).

First, we consider the selection effects that are inherent to the quasar distribution. Fig. 14 shows the distribution of quasars as a function of redshift z , i magnitude M_i , and black hole mass M_{BH} . For instance, the trend of increasing redshift with M_i on the upper left panel is due to the fact that quasars have to be brighter to be included in the survey at increasing distances.

As explained in (Shen et al. 2008, 2011), the most common approach to estimate quasar black hole mass is to assume that the broad-line region (BLR) is virialized, so that the continuum luminosity can be used as a proxy for the BLR radius, and the width of the broad emission lines (or line dispersion) is used to compute the virial velocity. The most commonly used, calibrated emission lines, that are available across different

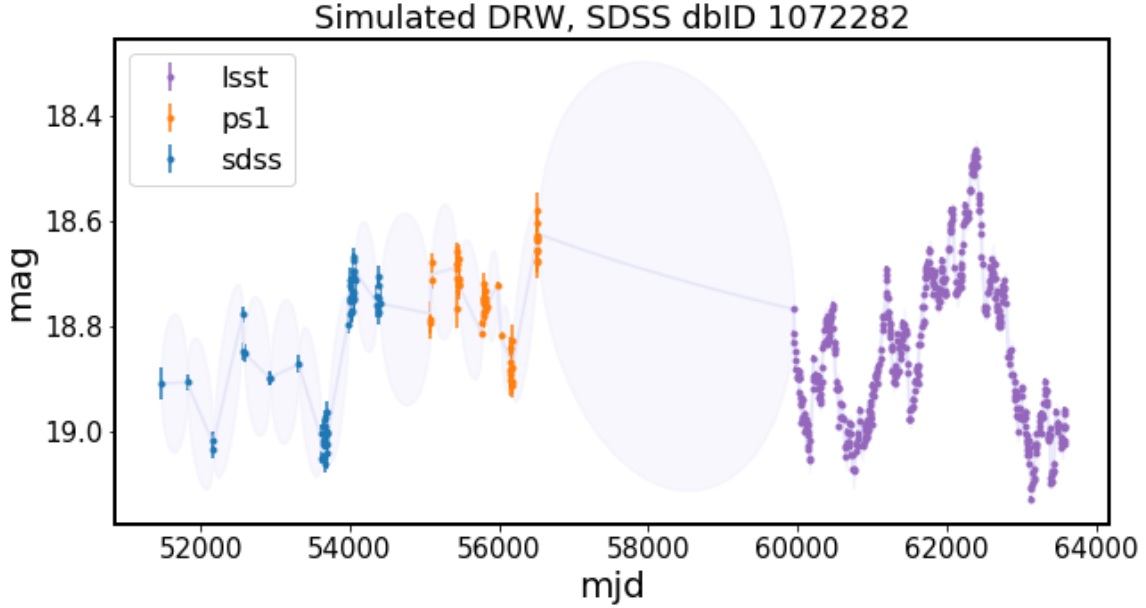


Figure 7. Simulated DRW process sampled at real cadence of SDSS, PS1, and simulated cadence of LSST. To each observed point we add Gaussian noise corresponding to the reported heteroscedastic (different for all points) errors for SDSS-PS1, and simulated magnitude-dependent errors for LSST.

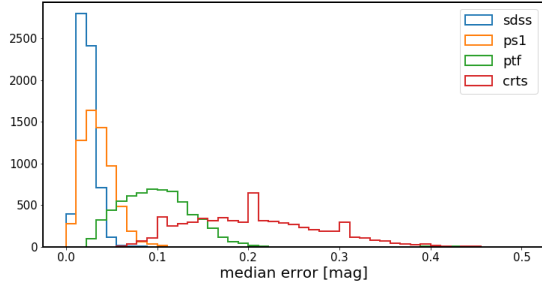


Figure 8. Distribution of median errors in combined r-band real light curves. We calculate the median per segment. This shows that the CRTS and PTF portions have much larger errors than SDSS, PS1, and are therefore less useful in improving the DRW parameters. This is the reason for using only SDSS-PS1 portion.

redshifts, are broad $H\alpha$, $H\beta$, $Mg II$, and $C IV$ (Vestergaard 2002). There are various available catalogs of quasar properties : redshift, absolute i-band luminosity, black hole mass. Usually the first quasar catalog releases basic properties such as redshift and photometry (eg. Schneider et al. 2007, 2010, and then more involved studies derive black hole masses and bolometric luminosities (eg. Shen et al. 2008, 2011). This is also the case for more recent work: once (Pâris et al. 2017) released SDSS DR12 Quasar Catalog (DR12Q), (Kozłowski, Szymon 2017) followed by estimating from photometry the monochromatic luminosities, and deriving black hole masses, and (Chen et al. 2018) added a detailed analysis of continuum luminosities in the $H\alpha$,

$H\beta$ regions for low-redshift quasars. Using the spectra from Chinese LAMOST survey (Dong et al. 2018) also sought to estimate virial black hole masses, and the results while consistent with (Shen et al. 2011), suffered from necessity to peg the non-calibrated spectra to SDSS photometry which was taken at a different epoch. For sources variable at ~ 0.2 mag level, such as quasars, the ideal is to use single-epoch calibrated spectra to estimate continuum luminosity, and find virial black hole masses using relationships based on the monochromatic fluxes and broad line widths. Even though Pâris et al. (2018) DR14Q is the most recent catalog, like (Pâris et al. 2017) it lacks black hole masses and bolometric luminosities, and (Kozłowski, Szymon 2017) bases his analysis on a SDSS photometry as a proxy for monochromatic luminosities rather than directly from the spectra. Of all available catalogs, (Shen et al. 2011) provides the best to date measurements of quasar black hole masses and monochromatic luminosities, based directly on the single-epoch spectra, and is therefore our choice.

The absolute i-band magnitude M_i is a good proxy for the bolometric luminosity (see Shen et al. 2008, Fig.2). M_i is derived from the observed i-band magnitude, by correcting for Galactic extinction, and K-correcting for the fact that at different redshifts different portions of the spectral energy distribution are observed by the telescope filter bandpass. Historically termed K-correction (Oke & Sandage 1968), $K(z)$ is defined as $m_{intrinsic} = m_{observed} - K(z)$. In the early 2000s the standard was to K-correct to redshift 0, but

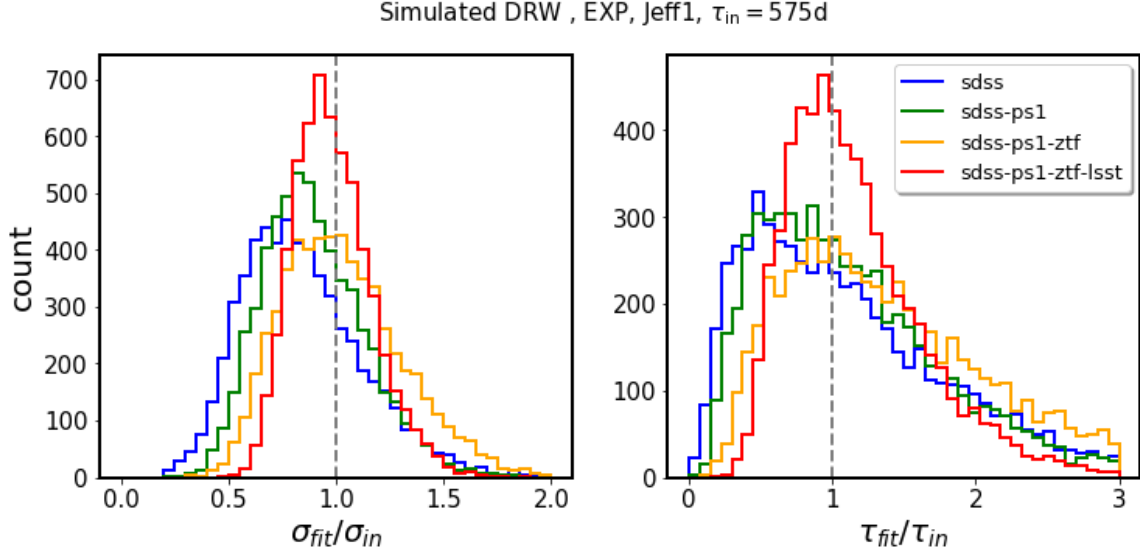


Figure 9. Retrieved τ and σ parameters for simulated LCs.

as (Richards et al. 2006) pointed out, since the distribution of quasars peaks at redshift 2, for most quasars $K(z=0)$ required shifting the observed spectrum into the far infrared. The procedure was to correct separately for the continuum and emission line contributions, assuming a particular spectral shape (eg. power law $f_\nu \propto \nu^\alpha$, with $\alpha = -0.5$ - see Schneider et al. 2010; Vanden Berk et al. 2001; Richards et al. 2006). This introduced large error if the assumed spectral shape $\alpha = -0.5$ was far from the real spectral index. In early 2010s the standard started to shift towards K-correcting to redshift 2 (following Richards et al. 2006; Wisotzki 2000; Blanton et al. 2003), and including custom quasar spectral shapes, as we see eg. in the catalog of (Shen et al. 2011). Thus in this study we use the absolute i-band magnitude K-corrected to $z=2$: $M_i(z=2)$ from (Shen et al. 2011).

We show on Fig. 15 τ and SF_∞ as a function of absolute magnitude M_i , redshift z , and black hole mass M_{BH} .

We investigate these correlations by fitting a power law, after MacLeod et al. (2011) :

$$\log_{10} f = A + B \log_{10} (\lambda_{RF}/4000\text{\AA}) + C(M_i + 23) + D \log_{10} (M_{BH}/10^9 M_\odot) \quad (15)$$

where f is τ_{RF} or SF_∞ .

MacLeod et al. (2011) used the Shen2008 catalog, and k-corrected the absolute i-band magnitude to a redshift of 0. Since then, given that the redshift distribution of quasars peaks at $z=2$, it has become a more standard practice to k-correct absolute quasar magnitudes to $z=2$, as it is in Shen2011 catalog. We opt to use Shen2011 catalog as a source of physical quasar parameters.

Since MacLeod et al. (2011) used independently fitted each of five SDSS bands, the coefficients A,C,D,E were band-averaged. The result of that, using the new data of Shen2011, is shown on Fig. 16

Since we used SDSS-PS1 combined r-band data, we compare the new DRW parameters to results of fitting MacLeod et al. (2011) r-band data (green line from Fig. 16).

The comparison of new results against old ones is shown on Fig. 18 and 17

Since the simulations showed that we do decrease the bias by extending the baseline, we use the combined SDSS-PS1 light curves and show the space occupied by quasars in $SF_\infty - \tau - \sigma$ space, which confirms the results of MacLeod et al. (2011) (Fig. ??)

REFERENCES

- AlSayyad, Y. 2016, PhD thesis, University of Washington.
<http://hdl.handle.net/1773/37020>
- Annis, J., Soares-Santos, M., Strauss, M. A., et al. 2014, ApJ, 794, 120, doi: [10.1088/0004-637X/794/2/120](https://doi.org/10.1088/0004-637X/794/2/120)
- Bauer, A., Baltay, C., Coppi, P., et al. 2009, ApJ, 696, 1241, doi: [10.1088/0004-637X/696/2/1241](https://doi.org/10.1088/0004-637X/696/2/1241)
- Blanton, M. R., Lin, H., Lupton, R. H., et al. 2003, AJ, 125, 2276, doi: [10.1086/344761](https://doi.org/10.1086/344761)

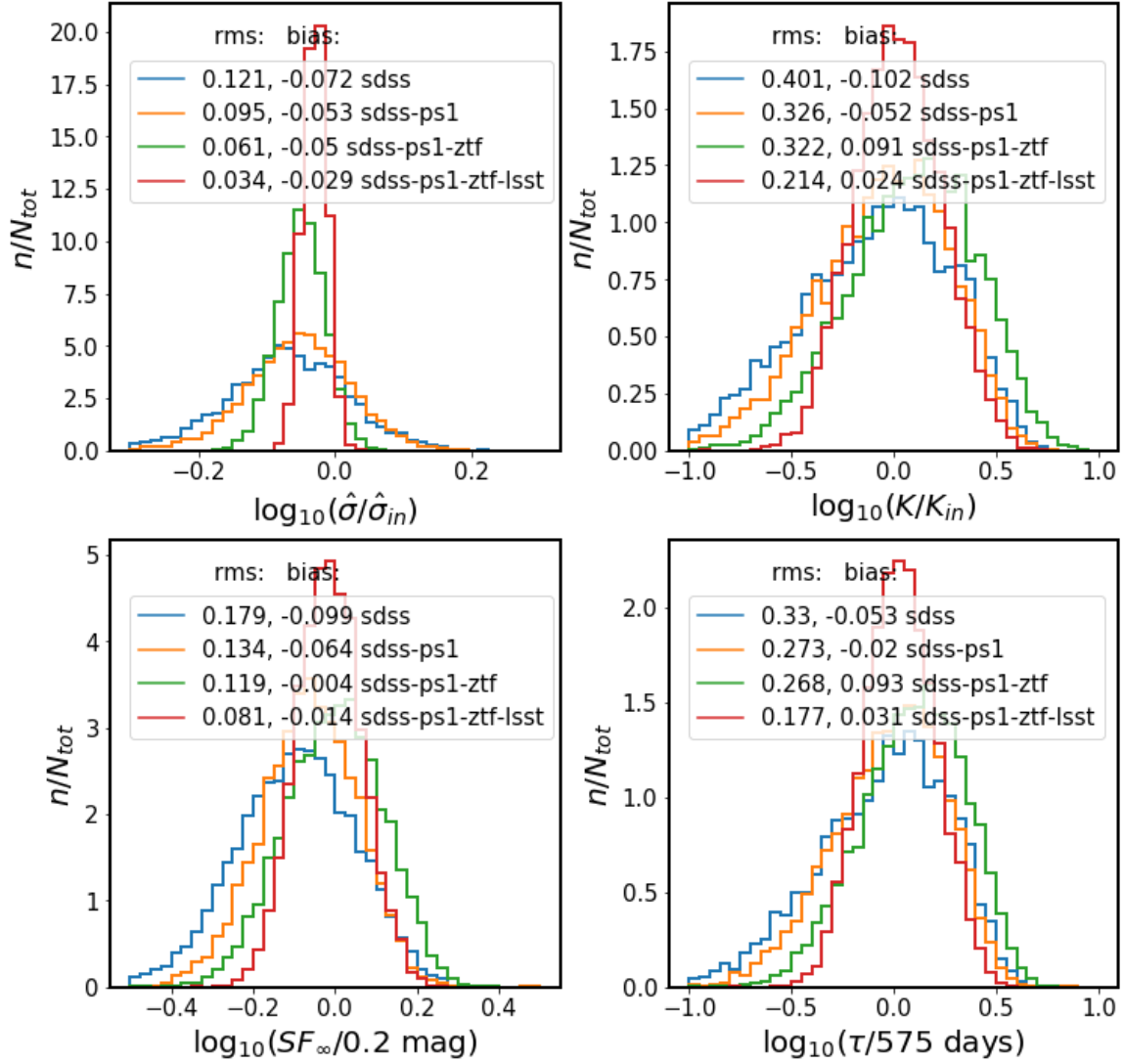


Figure 10. Comparison of retrieved parameters in relation to input parameters, shown as Fig.18 in MacLeod et al. (2011)

Chambers, K. C. 2011, in Bulletin of the American Astronomical Society, Vol. 43, American Astronomical Society Meeting Abstracts #218, 113.01

Chen, Z.-F., Pan, D.-S., Pang, T.-T., & Huang, Y. 2018, ApJS, 234, 16, doi: [10.3847/1538-4365/aa9d90](https://doi.org/10.3847/1538-4365/aa9d90)

Dexter, J., & Agol, E. 2011, ApJL, 727, L24, doi: [10.1088/2041-8205/727/1/L24](https://doi.org/10.1088/2041-8205/727/1/L24)

Dexter, J., & Begelman, M. C. 2019, MNRAS, 483, L17, doi: [10.1093/mnrasl/sly213](https://doi.org/10.1093/mnrasl/sly213)

Dong, X. Y., Wu, X.-B., Ai, Y. L., et al. 2018, AJ, 155, 189, doi: [10.3847/1538-3881/aab5ae](https://doi.org/10.3847/1538-3881/aab5ae)

Drake, A. J., Djorgovski, S. G., Mahabal, A., et al. 2009, ApJ, 696, 870, doi: [10.1088/0004-637X/696/1/870](https://doi.org/10.1088/0004-637X/696/1/870)

Flewelling, H. 2018, in American Astronomical Society Meeting Abstracts, Vol. 231, American Astronomical Society Meeting Abstracts 231, 436.01

Foreman-Mackey, D., Agol, E., Angus, R., & Ambikasaran, S. 2017, ArXiv e-prints, <https://arxiv.org/abs/1703.09710>

Graham, M. J., Djorgovski, S. G., Stern, D., et al. 2015, Nature, 518, 74, doi: [10.1038/nature14143](https://doi.org/10.1038/nature14143)

Guo, H., Wang, J., Cai, Z., & Sun, M. 2017, ApJ, 847, 132, doi: [10.3847/1538-4357/aa8d71](https://doi.org/10.3847/1538-4357/aa8d71)

Hernitschek, N., Schlafly, E. F., Sesar, B., et al. 2016, The Astrophysical Journal, 817, 73

Ivezić, Ž., Smith, J. A., Miknaitis, G., et al. 2007, AJ, 134, 973, doi: [10.1086/519976](https://doi.org/10.1086/519976)

Kasliwal, V. P., Vogeley, M. S., & Richards, G. T. 2015, MNRAS, 451, 4328, doi: [10.1093/mnras/stv1230](https://doi.org/10.1093/mnras/stv1230)

Kelly, B. C., Bechtold, J., & Siemiginowska, A. 2009, The Astrophysical Journal, 698, 895

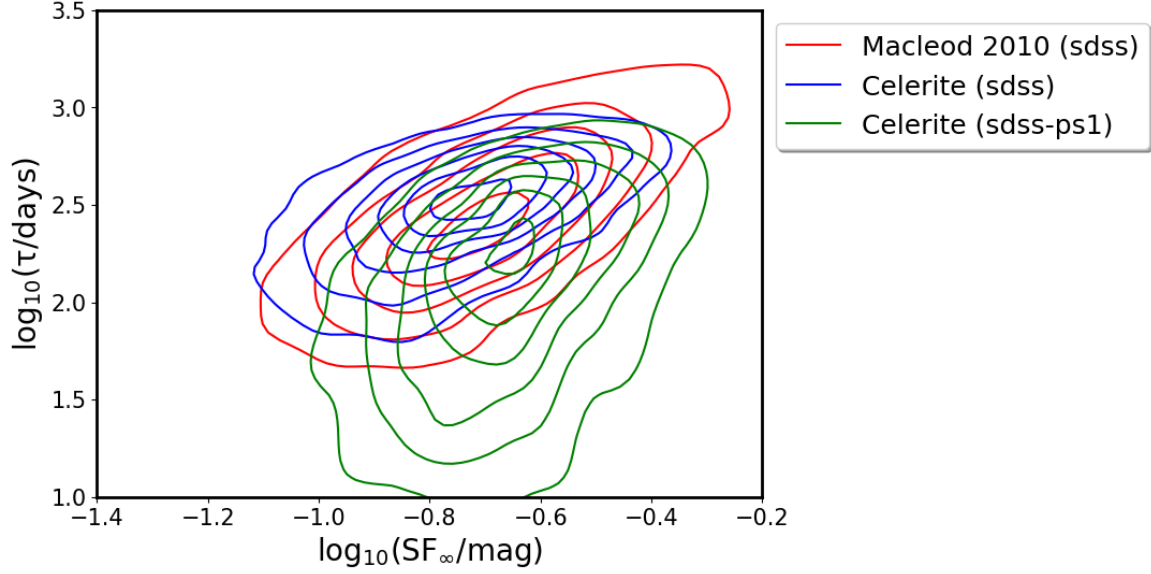


Figure 11. Comparing the rest-frame timescales τ , and asymptotic variability amplitudes SF_{∞} , for MacLeod et al. (2011) SDSS r-band, and combined SDSS and PS1 data.

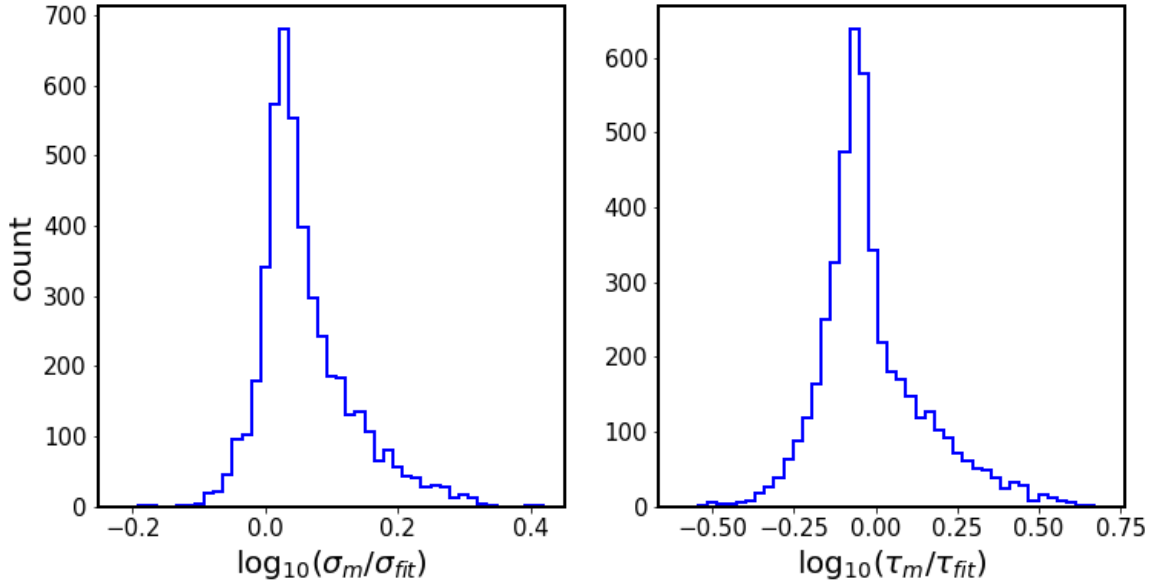


Figure 12. Plot comparing results for SDSS r-band fitting of MacLeod et al. (2011) (σ_m, τ_m), and current results for SDSS r-band using Celerite (σ_{fit}, τ_{fit}).

Kelly, B. C., Treu, T., Malkan, M., Pancoast, A., & Woo, J.-H. 2013, *ApJ*, 779, 187,
doi: [10.1088/0004-637X/779/2/187](https://doi.org/10.1088/0004-637X/779/2/187)
Kozłowski, S., Kochanek, C. S., Udalski, A., et al. 2010, *ApJ*, 708, 927
Kozłowski, Szymon. 2017, *A&A*, 597, A128,
doi: [10.1051/0004-6361/201629890](https://doi.org/10.1051/0004-6361/201629890)
Kubota, A., & Done, C. 2018, *MNRAS*, 480, 1247,
doi: [10.1093/mnras/sty1890](https://doi.org/10.1093/mnras/sty1890)

Li, Z., McGreer, I. D., Wu, X.-B., Fan, X., & Yang, Q. 2018, *ApJ*, 861, 6, doi: [10.3847/1538-4357/aac6ce](https://doi.org/10.3847/1538-4357/aac6ce)
LSST Science Collaboration, Abell, P. A., Allison, J., et al. 2009, arXiv e-prints, arXiv:0912.0201.
<https://arxiv.org/abs/0912.0201>
MacLeod, C. L., Ivezić, Ž., Kochanek, C. S., et al. 2010, *The Astrophysical Journal*, 721, 1014
MacLeod, C. L., Brooks, K., Ivezić, Ž., et al. 2011, *The Astrophysical Journal*, 728, 26

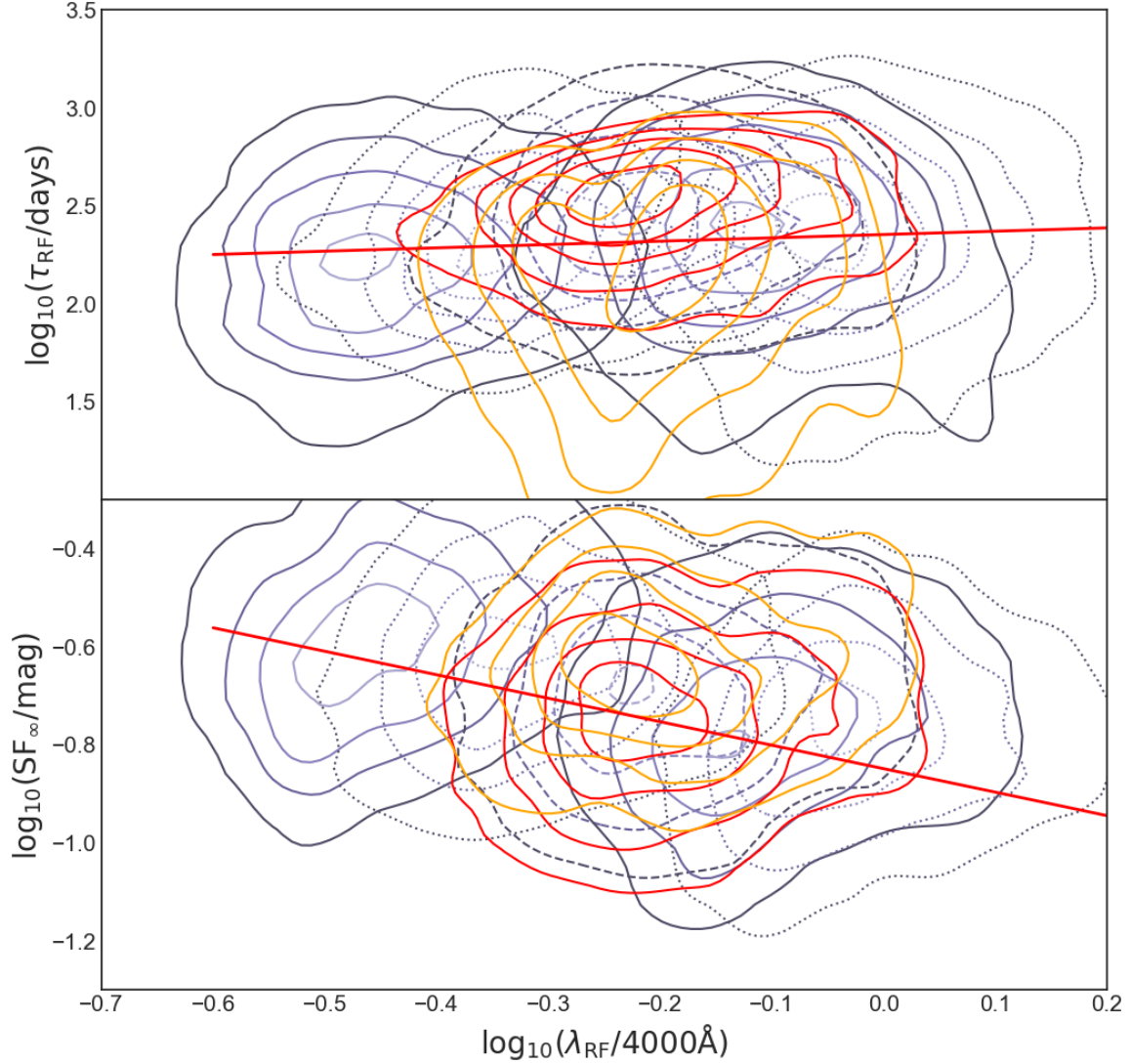


Figure 13. Rest-frame timescale τ (top panel), and long-term structure function SF_{∞} (bottom panel), as a function of rest-frame wavelength λ_{RF} . The background contours show MacLeod et al. (2011) SDSS ugriz data, and the foreground contours denote the SDSS (red) and SDSS-PS1 (orange) new results with Celerite. In all datasets the quasars were selected according to criteria of MacLeod et al. (2011). The red line indicates the best-fit power law to MacLeod et al. (2011) data, with $B = 0.17$ an -0.479 for τ_{RF} , and SF_{∞} , respectively.

MacLeod, C. L., Ivezić, Ž., Sesar, B., et al. 2012, The Astrophysical Journal, 753, 106

McGreer, I. D., Fan, X., Jiang, L., & Cai, Z. 2018, AJ, 155, 131, doi: [10.3847/1538-3881/aaaab4](https://doi.org/10.3847/1538-3881/aaaab4)

McGreer, I. D., Jiang, L., Fan, X., et al. 2013, ApJ, 768, 105, doi: [10.1088/0004-637X/768/2/105](https://doi.org/10.1088/0004-637X/768/2/105)

Oke, J. B., & Sandage, A. 1968, ApJ, 154, 21, doi: [10.1086/149737](https://doi.org/10.1086/149737)

Palanque-Delabrouille, N., Magneville, C., Yèche, C., et al. 2013, A&A, 551, A29, doi: [10.1051/0004-6361/201220379](https://doi.org/10.1051/0004-6361/201220379)

Pâris, I., Petitjean, P., Ross, N. P., et al. 2017, A&A, 597, A79, doi: [10.1051/0004-6361/201527999](https://doi.org/10.1051/0004-6361/201527999)

Pâris, I., Petitjean, P., Aubourg, É., et al. 2018, A&A, 613, A51, doi: [10.1051/0004-6361/201732445](https://doi.org/10.1051/0004-6361/201732445)

Rau, A., Kulkarni, S. R., Law, N. M., et al. 2009, PASP, 121, 1334, doi: [10.1086/605911](https://doi.org/10.1086/605911)

Richards, G. T., Strauss, M. A., Fan, X., et al. 2006, AJ, 131, 2766, doi: [10.1086/503559](https://doi.org/10.1086/503559)

Ross, N. P., McGreer, I. D., White, M., et al. 2013, ApJ, 773, doi: [10.1088/0004-637X/773/1/14](https://doi.org/10.1088/0004-637X/773/1/14)

Rybicki, G. B., & Press, W. H. 1992, ApJ, 398, 169, doi: [10.1086/171845](https://doi.org/10.1086/171845)

Sánchez-Sáez, P., Lira, P., Mejía-Restrepo, J., et al. 2018, ApJ, 864, 87, doi: [10.3847/1538-4357/aad7f9](https://doi.org/10.3847/1538-4357/aad7f9)

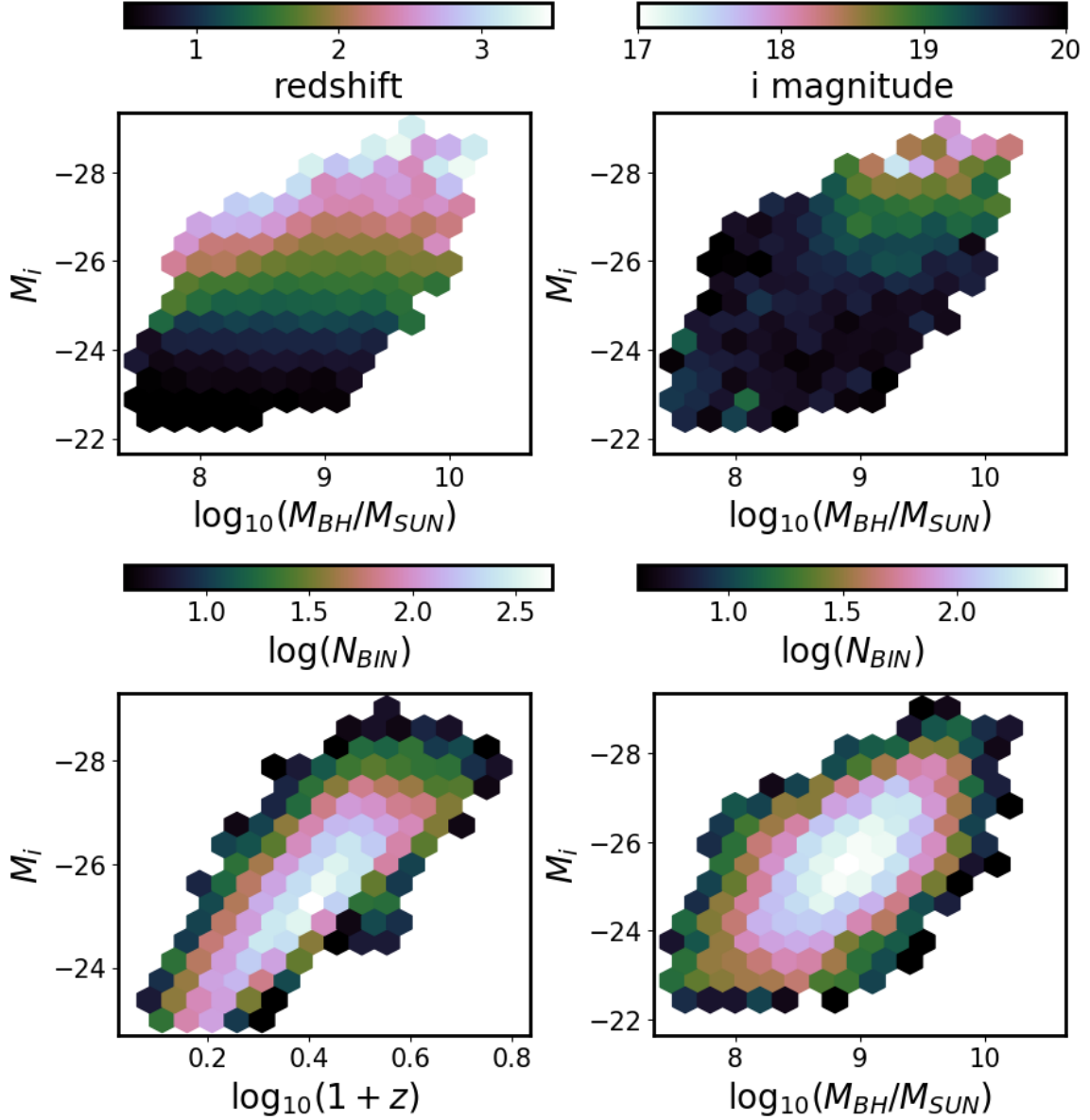


Figure 14. Distribution of quasars as a function of redshift, observed i-band magnitude, absolute i-band magnitude (K-corrected to $z=2$), and virial black hole mass. All quantities from (Shen et al. 2011).

Schneider, D. P., Hall, P. B., Richards, G. T., et al. 2007, AJ, 134, 102, doi: [10.1086/518474](https://doi.org/10.1086/518474)

—. 2008, VizieR Online Data Catalog, 7252

Schneider, D. P., Richards, G. T., Hall, P. B., et al. 2010, AJ, 139, 2360, doi: [10.1088/0004-6256/139/6/2360](https://doi.org/10.1088/0004-6256/139/6/2360)

Sesar, B., Ivezić, Ž., Lupton, R. H., et al. 2007, AJ, 134, 2236

Shen, Y., Greene, J. E., Strauss, M. A., Richards, G. T., & Schneider, D. P. 2008, ApJ, 680, 169, doi: [10.1086/587475](https://doi.org/10.1086/587475)

Shen, Y., Richards, G. T., Strauss, M. A., et al. 2011, ApJS, 194, 45, doi: [10.1088/0067-0049/194/2/45](https://doi.org/10.1088/0067-0049/194/2/45)

Sun, M., Xue, Y., Wang, J., Cai, Z., & Guo, H. 2018, ApJ, 866, 74, doi: [10.3847/1538-4357/aae208](https://doi.org/10.3847/1538-4357/aae208)

Tonry, J. L., Stubbs, C. W., Lykke, K. R., et al. 2012, ApJ, 750, 99, doi: [10.1088/0004-637X/750/2/99](https://doi.org/10.1088/0004-637X/750/2/99)

Vanden Berk, D. E., Richards, G. T., Bauer, A., et al. 2001, AJ, 122, 549, doi: [10.1086/321167](https://doi.org/10.1086/321167)

Vestergaard, M. 2002, ApJ, 571, 733, doi: [10.1086/340045](https://doi.org/10.1086/340045)

Wisotzki, L. 2000, A&A, 353, 861

Yang, J., Fan, X., Wu, X.-B., et al. 2017, AJ, 153, 184, doi: [10.3847/1538-3881/aa6577](https://doi.org/10.3847/1538-3881/aa6577)

Zu, Y., Kochanek, C. S., & Peterson, B. M. 2011, ApJ, 735, 80

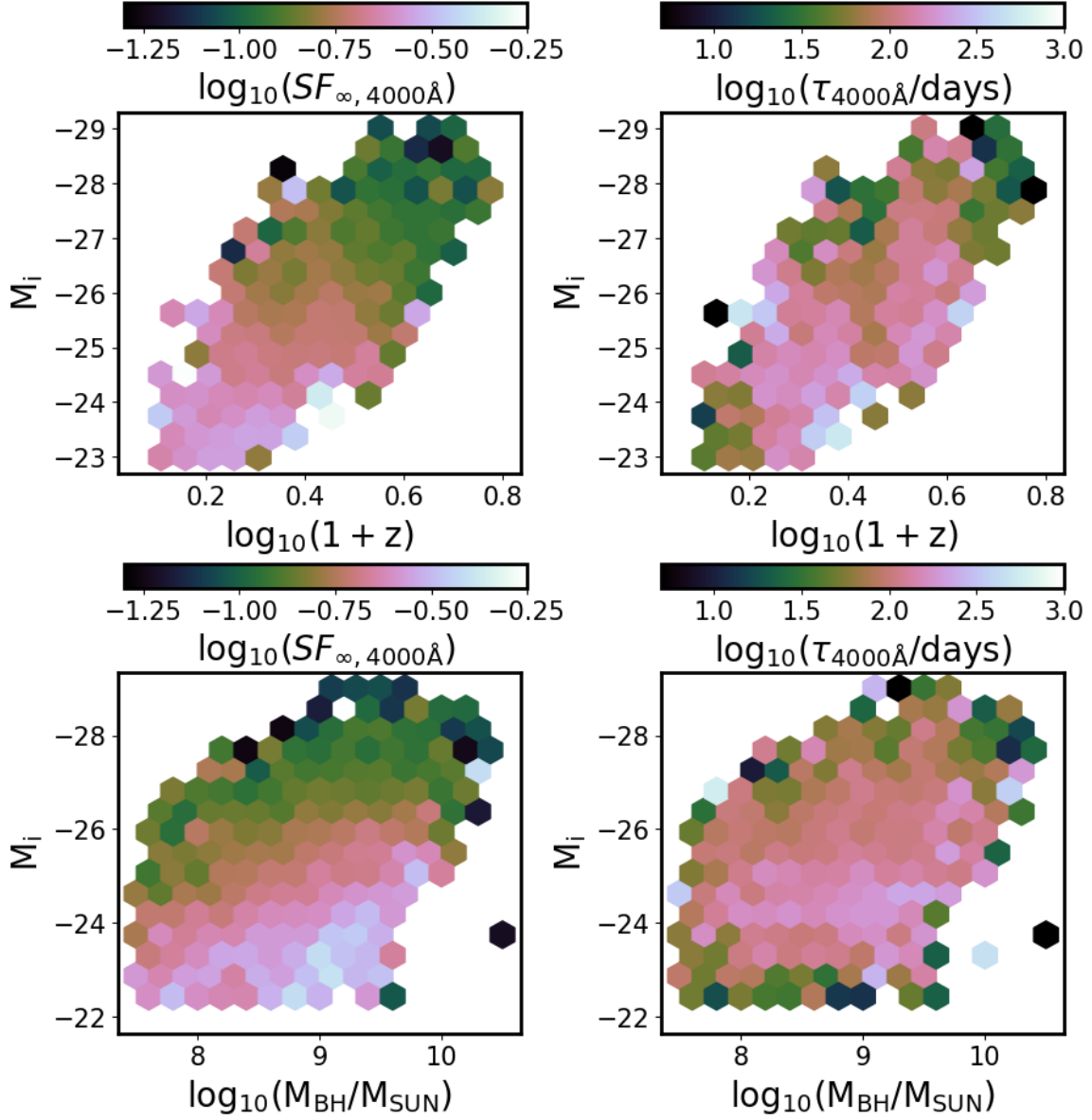


Figure 15. Long-term variability (SF_{∞}), and characteristic timescale (τ), as a function of absolute i-band magnitude (K-corrected to redshift 2, proxy for bolometric luminosity), virial black hole mass, and redshift.

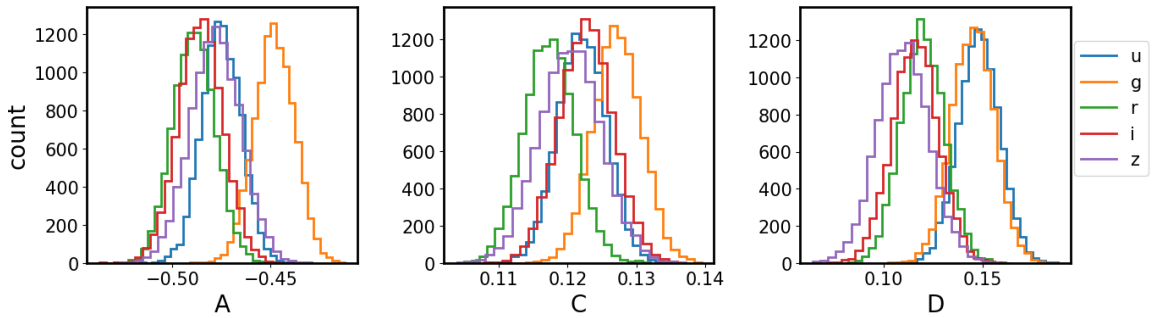


Figure 16. Samples from posterior MCMC draws for fit coefficients A,C,D (setting E=0), using Shen2011 values for redshift, absolute i-band magnitude, black hole mass. The vertical dashed line marks the band-averaged values for fit coefficients.

Table 1. Color terms (offsets) between the following survey filters and SDSS(r) band, using the mean SDSS(g-i) color, so that the synthetic SDSS(r) magnitude can be found as $r_{SDSS,synth} = x - B_0 - B_1 SDSS(g-i)$

Band (x)	B_0	B_1
CRTS V	-0.0464	-0.0128
PTF g	-0.0294	0.6404
PTF R	0.0058	-0.1019
PS1 g	0.0194	0.6207
PS1 r	0.0057	-0.0014
PS1 i	0.0247	-0.2765

NOTE—To derive the offsets we used SDSS S82 1 mln standard stars catalog (Ivezić et al. 2007). We randomly selected 10% of that catalog, for which 48250 have CRTS light curves with at least 10 observations (B.Sesar). For these stars we obtained PS1 photometry from MAST <http://panstarrs.stsci.edu> and PTF from IRSA PTF Object Catalog <https://irsa.ipac.caltech.edu/>. We further imposed quality cuts requiring that the stars are bright: $r < 19$.

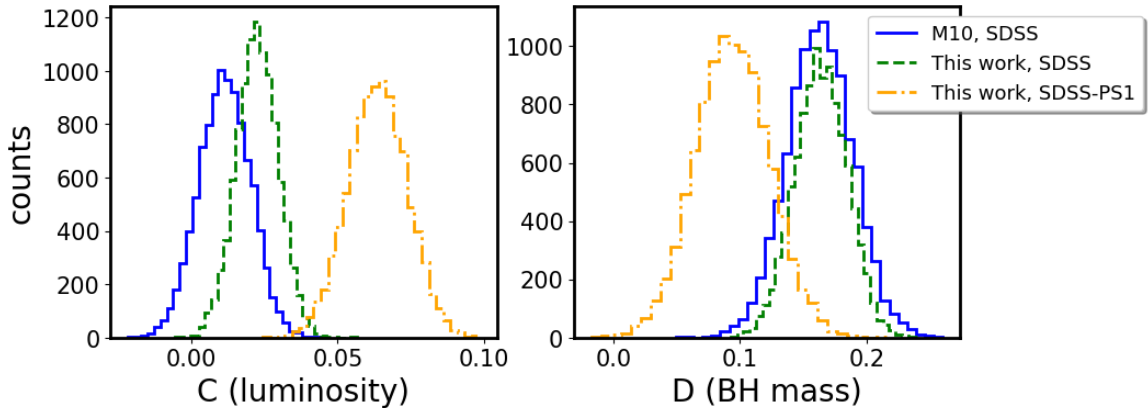


Figure 17. Comparison of Celerite fits of SDSS, SDSS-PS1 portions of combined quasar light curves against MacLeod et al. (2011) results of SDSS r-band only. The results from SDSS-only portion are consistent with previous results, and inclusion of the PS1 portion that increases the baseline decreases the timescale dependence on black hole mass, but increases the luminosity dependence. This can be understood as a rotation of the plane in (τ, M_i, M_{BH}) coordinates.

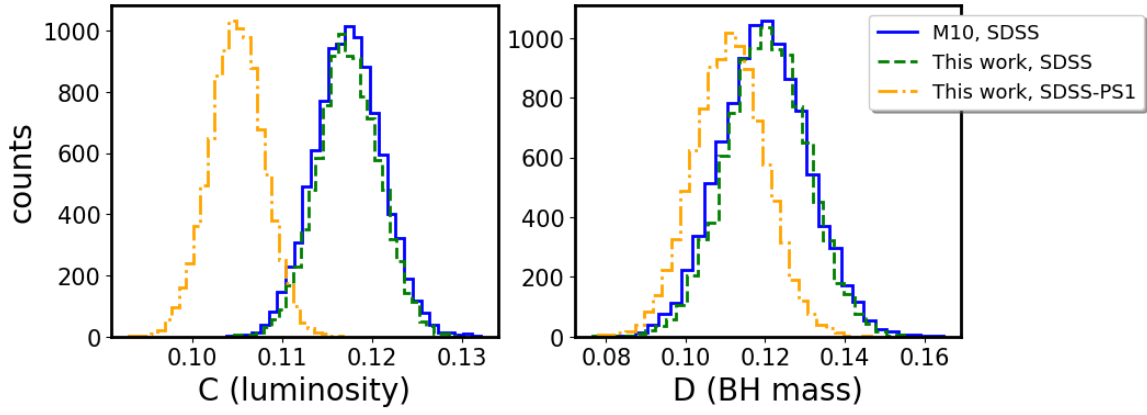


Figure 18. Same as Fig. 17, but showing the asymptotic amplitude SF_{∞} . New data from PS1 supports a weaker dependence of variability amplitude with luminosity and black hole mass (using Shen2011 data).